Centralized Autonomous Relative Navigation of Multiple Cubesats around Didymos System

Stefano Silvestrini · Margherita Piccinin · Andrea Capannolo · Michèle Lavagna · Jesus Gil Fernandez

Received: date / Accepted: date

Abstract This paper presents an on-board, centralized autonomous navigation algorithm able to reconstruct the trajectories of a fleet of CubeSats relative to an asteroid binary system. The algorithm is executed on-board the main spacecraft, which takes relative measurements using a narrow optical camera and an additional relative measurement, being inter satellite ranging in this paper. The image processing algorithm detects and tracks the CubeSats, deriving line-of-sight measurements. A non-linear estimation filter is employed to reconstruct the trajectory. The algorithm is tested using high-fidelity trajectory simulator and synthetic images generation routines.

Keywords Autonomous navigation · Vision-based · HERA mission · Didymos · Vision-based

Presented at the AIAA Scitech 2020 Forum
ESA RFP/ 3-16012/19/NL/CRS/hh-19.3EC.04

Corresponding author, Politecnico di Milano
Via La Masa 34, 20156, Milano, Italy
E-mail: stefano.silvestrini@polimi.it

Politecnico di Milano
Via La Masa 34, 20156, Milano, Italy
E-mail: margherita.piccinin@polimi.it

Politecnico di Milano
Via La Masa 34, 20156, Milano, Italy
E-mail: andrea.capannolo@polimi.it

Politecnico di Milano
Via La Masa 34, 20156, Milano, Italy
E-mail: michelle.lavagna@polimi.it

European Space Agency, ESTEC
Keplerlaan 1, 2201 AZ Noordwijk, The Netherlands
E-mail: Jesus.Gil.Fernandez@esa.int

1 Introduction

Recent interest in small celestial objects, such as asteroids and comets, is pushing towards the design of new missions to explore such ancient bodies of the Solar System. This is justified not only by the scientific breakthrough they may lead to, but also by the hazard they may pose to Earth. In such context, it is desirable to get as close as possible to these objects, although the low and irregular gravitational environment make their surroundings dangerous to explore.

A workaround to this problem is being considered by exploiting small and expendable satellites as scouts, to perform close range and risky operations. It is the case of NASA's "DART" (Double Asteroid Redirection Test) mission, which will impact the moonlet of a small binary asteroid system called 65803 Didymos, to perform a miniaturized test of asteroid deflection through kinetic impactor [9,1]. While the American spacecraft will be destroyed at the impact, it will carry a small CubeSat (LICIACube-Light Italian CubeSat for Imaging of Asteroids), which will be deployed before the impact and will flyby the system to gather additional scientific information about the bodies [6,11]. ESA will give a major contribution to the study of Didymos system, by sending the Hera spacecraft, which will stay in the asteroids' surroundings for a longer time to fully characterize the two celestial objects. Two CubeSats, Apex and Juventas, will be carried and released to get closer to the system. Such strategy allows the main spacecraft to stay safe, maneuvering relatively far from the target bodies, while the CubeSats engage in riskier operations that yield high-value scientific data. However, the longer permanence in this environment tightens the accuracy required from navigation.

The paper considers the possibility of exploiting a centralized autonomous navigation for these spacecraft, where the optical navigation capability of Hera spacecraft is exploited to detect and track the CubeSats [17]. This strategy would reduce the cost and complexity of the ground operations of deep space CubeSats, exploiting the mothercraft already existing autonomous navigation capability. Autonomous navigation is currently being developed for deep space mission but it still relies on on-ground determination backup [17]. The high-level of complexity, due to the peculiar dynamical environment and the limited authority on central navigation, poses several problems for an effective navigation strategy. In particular, typical optical Line-Of-Sight (LOS) measurements are taken by tracking the desired object using also the orbital/attitude control of the spacecraft [17,20]. An integrated Image Processing (IP) coupled with estimation algorithms are usually employed for deep space navigation, as reported in [17,27]. For instance, AutoNav, developed by the Jet Propulsion Laboratory, currently uses a set of IP techniques coupled with a batch-sequential filter estimation scheme [31]. The state-of-the-art techniques require a considerable computational power and a nearly complete control authority of the spacecraft. These architectures, although high-performing, are not suitable for the examined scenario due to the following considerations:

- the proposed centralized navigation does not have any control authority on the spacecraft, meaning that the processed images are not acquired specifically to carry out the CubeSats relative navigation;
- the CubeSats are small and far from the Hera spacecraft, hence a limited number of IP techniques can be applied;

– the CubeSats centralized relative navigation shall have a very limited computational burden to be deployed alongside the main Hera navigation.

The paper major contribution is to propose and assess the feasibility of an onboard centralized estimation algorithm, using LOS and ranging measurements, to estimate the trajectory of Apex and Juventas CubeSats around the Didymos system. The navigation algorithm obtains a fully observable solution from the low-observability sensor measurements in the presence of large dynamics uncertainties and measurement non-linearities.

The paper is structured as follows. Section 2 describes the definition of the scenario together with the high-fidelity orbital simulator used for generating the reference trajectories. Section 3 discusses the alternatives and the trade-offs performed for the image processing algorithm, focusing on the baseline detailed implementation. Section 4 discusses the trade-off performed among the alternatives and describes the estimation algorithm based on the Extended Schmidt-Kalman Filter. Finally, Section 5 reports the preliminary results of the whole navigation algorithm in the nominal scenario.

2 Scenario Definition

2.1 Target system: 65803 Didymos

Didymos is a S-type binary asteroid system, belonging to the Near Earth Asteroids (NEA) group [26,30]. It consists of a larger main object, called "Didymain", and a moonlet orbiting around it, called "Dimorphos".

Didymain is characterized by a nearly-spherical shape, and has an equivalent radius of 780 m. Dimorphos is too small for its shape to be accurately reconstructed, and it is approximated as a triaxial ellipsoid, having a semi-major axis of around 100 m and a semi-minor axis of 65 m. Dimorphos orbits around Didymain at a mean distance of 1180 m, with an eccentricity of 0.03 (highest estimated value) and a corresponding period of 11.9 h. The moonlet is tidally locked to the primary attractor, hence its spin is resonant with its orbital period around the primary, while Didymain displays a faster spin, making one rotation every 2.26 h. Both asteroids are assumed to have the same composition and the same density, around $2170\,\mathrm{kg\,m^{-3}}$. Fig. 1 depicts the system with up-to-date reconstructed shapes and dimensions.

2.2 Dynamics

The section introduces the dynamical models adopted in the process of generating and refining the reference trajectories of all the spacecraft involved.

Keplerian model The simpler model adopted for the present analysis considers the whole binary system as a point mass, with a mass given by the sum of the two attractors' masses. The equations of motion read:

$$\ddot{\mathbf{r}} = -\frac{Gm}{\|\mathbf{r}\|^3}\mathbf{r} + \mathbf{f_d} \tag{1}$$

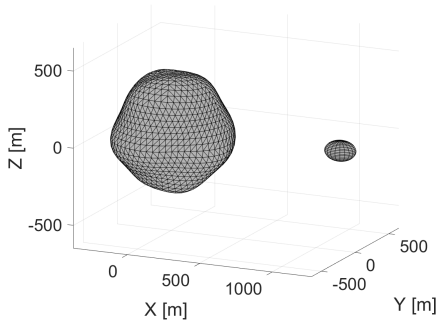

Fig. 1: 65803 Didymos binary system.

where $\mathbf{r}$ is the relative position of the orbiting object with respect to the attractor, $\ddot{\mathbf{r}}$ is its second derivative over time, m is the attractor's mass, and G is the gravitational constant. $\mathbf{f_d}$ represents the overall disturbance accelerations, at it equals zero in the unperturbed dynamics model.

Circular Restricted Three Body Problem (CRTBP) The next level of complexity for the dynamics considers the two attractors as separated bodies, orbiting around each other according to the Keplerian law (Eq. 1), and describing circular orbits. As a consequence, their rotation frequency and mutual distance are constant, and it is convenient to express the equations of motion in a synchronized, synodic, nondimensional frame [22]:

$$\ddot{\mathbf{r}} = \begin{bmatrix} 1 & 0 & 0 \\ 0 & 1 & 0 \\ 0 & 0 & 0 \end{bmatrix} \mathbf{r} - 2 \begin{bmatrix} 0 & -1 & 0 \\ 1 & 0 & 0 \\ 0 & 0 & 0 \end{bmatrix} \dot{\mathbf{r}} + \mathbf{f_{g1}^P} + \mathbf{f_{g2}^P} + \mathbf{f_d} \tag{2}$$

with $\mathbf{r}$,$\dot{\mathbf{r}}$, and $\ddot{\mathbf{r}}$ representing the relative position of the spacecraft with respect to the binary system's center of mass, and its first and second derivative over time respectively. Here, $\mathbf{f_{g1}^P}$ and $\mathbf{f_{g2}^P}$ are the point mass gravitational accelerations arising from the primary and the secondary attractor respectively, and are expressed as:

$$\begin{aligned} \mathbf{f_{g1}^P} &= -\frac{(1-\mu)}{\|\mathbf{r_1}\|^3}\mathbf{r_1} \\ \mathbf{f_{g2}^P} &= -\frac{\mu}{\|\mathbf{r_2}\|^3}\mathbf{r_2} \end{aligned} \tag{3}$$

with μ being the ratio between secondary mass and overall system mass ($\frac{m_2}{m_1+m_2}$), and $\mathbf{r_1}$ and $\mathbf{r_2}$ the relative positions of the spacecraft with respect to the primary and secondary attractors, expressed as:

$$\begin{aligned} \mathbf{r_1} &= \begin{Bmatrix} x+\mu \\ y \\ z \end{Bmatrix} \\ \mathbf{r_2} &= \begin{Bmatrix} x+(\mu-1) \\ y \\ z \end{Bmatrix} \end{aligned} \tag{4}$$

As in Eq. 1, $\mathbf{f_d}$ is zero in the unperturbed dynamics.

Elliptic Restricted Three Body Problem (ERTBP) To further generalize the dynamics, Eq. 2 can be modified to assume an elliptic orbit for the two attractors. Such assumption make the characteristic quantities (orbital frequency and distance) no longer constant, and their variation must be included in the equation of motion through the eccentric anomaly parameter (E) [33]:

$$\begin{cases} \ddot{\mathbf{r}} & = n^2 \begin{bmatrix} 1 & 0 & 0 \\ 0 & 1 & 0 \\ 0 & 0 & 0 \end{bmatrix} \mathbf{r} - \begin{bmatrix} 0 & -1 & 0 \\ 1 & 0 & 0 \\ 0 & 0 & 0 \end{bmatrix} (2n\dot{\mathbf{r}} + \dot{n}\mathbf{r}) + \mathbf{f_{g1}^P} + \mathbf{f_{g2}^P} + \mathbf{f_d} \\ \dot{E} & = \frac{1}{1 - e\cos E} \end{cases} \tag{5}$$

where e is the eccentricity of attractors' orbits, and n and $\dot{n}$ are the nondimensional, time variant angular rate and its derivative, defined as:

$$\begin{aligned} n &= \frac{\sqrt{1-e^2}}{(1-e\cos E)^2} \\ \dot{n} &= -2e\frac{\sqrt{1-e^2}}{(1-e\cos E)^4}\sin E \end{aligned} \tag{6}$$

$\mathbf{f_{g1}^P}$ and $\mathbf{f_{g2}^P}$ maintain the same expression as in Eq. 3, however, the relative positions vectors from Eq. 4 are corrected according to the new dynamics model, and read:

$$\begin{aligned} \mathbf{r_1} &= \begin{Bmatrix} x + \mu(1 - e\cos E) \\ y \\ z \end{Bmatrix} \\ \mathbf{r_2} &= \begin{Bmatrix} x + (\mu - 1)(1 - e\cos E) \\ y \\ z \end{Bmatrix} \end{aligned} \tag{7}$$

As in Eq. 1 and Eq. 2, $\mathbf{f_d}$ is null in absence of external perturbations.

Shape-based Circular/Elliptic Restricted Three Body Problem (SCRTBP / SERTBP) Eq. 2 and Eq. 5 are built around the assumption of perfectly spherical (or equivalently, point mass) attractors. A modified formulation of the aforementioned equations is built, to take into account the uneven shape of the attractors, and hence their irregular gravity field.

The main attractor's shape is well known from ground observation, and a high fidelity model has been developed and used in several research studies [5, 4, 14, 15, 10], according to the gravity field expression from a polyhedral object [34]. It was observed that an axisymmetric representation of the asteroid, based on harmonic expansion and Legendre polynomials up to the seventh order [2], provides a very good approximation of the high fidelity gravity field [3], and inherently takes into account the fast natural spin of the body. The expression of the gravitational potential through spherical harmonics, for the axisymmetric body, reads:

$$U_1^{sh} = \frac{Gm_1}{\|\mathbf{r_1}\|} + \sum_{k=1}^{\infty} \frac{A_k}{\|\mathbf{r_1}\|^{k+1}} P_k(\cos\phi) \tag{8}$$

where m_1 is the mass of the primary attractor, P_k is the kth-degree Legendre's polynomial, ϕ is the colatitude of the spacecraft relative to the attractor's surface, and A_k is a coefficient defined as:

$$A_k = 2\pi G\rho \int_S r_s^{k+2} P_k(\cos\phi_s)\sin\phi_s dS \tag{9}$$

with ρ being the density of the body, r_s the local radius of the body's surface, and ϕ_s the local colatitude. Then, the corresponding gravity acceleration term $\mathbf{f_{g1}^{sp}}$, reads:

$$\mathbf{f_{g1}^{sh}} = \nabla U_1^{sh} \tag{10}$$

The secondary attractor is too small for a satisfactory shape reconstruction from ground, and little information on the shape is available. For this reason, it was modeled as a triaxial ellipsoid, tidally locked to the main asteroid. The simpler shape facilitated the use of a dedicated expression for the gravity field, exploiting elliptic integrals of first and second kind [25]. The potential for a triaxial ellipsoid reads:

$$\begin{aligned} U_2^{ell} =& \frac{2G\rho\pi abc}{\sqrt{a^2-c^2}}\Bigg\{\left[1-\frac{x^2}{a^2-b^2}+\frac{y^2}{a^2-b^2}\right]F(\omega_\kappa,k)+ \\ &+\left[\frac{x^2}{a^2-b^2}-\frac{(a^2-c^2)y^2}{(a^2-b^2)(b^2-c^2)}+\frac{z^2}{b^2-c^2}\right]E(\omega_\kappa,k)+ \\ &+\left[\frac{(c^2+\kappa)y^2}{b^2-c^2}-\frac{(b^2+\kappa)z^2}{b^2-c^2}\right]\frac{\sqrt{a^2-c^2}}{\sqrt{(a^2+\kappa)(b^2+\kappa)(c^2+\kappa)}}\Bigg\} \end{aligned} \tag{11}$$

where a,b, and c are the three semi-axes of the body (sorted from largest to smallest), $F(\omega_\kappa,k)$ and $E(\omega_\kappa,k)$ are the elliptic integrals of first and second kind, and ω_κ, k and κ are defined such that the following equations are satisfied:

$$\begin{aligned} &\frac{x^2}{a^2+\kappa}+\frac{y^2}{b^2+\kappa}+\frac{z^2}{c^2+\kappa}=1 \\ &k^2=\frac{a^2-b^2}{a^2-c^2} \\ &\omega_\kappa=\sin^{-1}\left(\sqrt{\frac{a^2-c^2}{a^2+\kappa}}\right) \end{aligned} \tag{12}$$

The corresponding gravity acceleration reads:

$$\mathbf{f_{g2}^{ell}} = \nabla U_2^{ell} \tag{13}$$

Both bodies were assumed to have a constant density, with physical properties derived from ground observations [12]. The new formulations of the gravity field, $\mathbf{f_{g1}^{sh}}$ and $\mathbf{f_{g2}^{ell}}$, are substituted to the right-hand side gravity terms $\mathbf{f_{g1}^{p}}$ and $\mathbf{f_{g2}^{p}}$ respectively, in both dynamics expressions of Eq. 2 and Eq. 5.

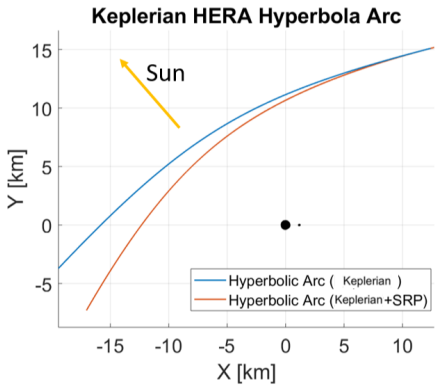

Fig. 2: SRP effect on Hera's trajectory.

Solar radiation pressure (SRP) Due to the low gravity field of the binary system, the SRP effect on spacecraft orbits gains a non-negligible effect also in a short time fashion. The perturbative acceleration coming from solar particles can be modeled as:

$$\mathbf{f_s} = -p_s C_R \frac{A}{m} \hat{\mathbf{r}}_{\mathbf{Sun}} \tag{14}$$

where p_s is the luminosity of the Sun, C_R is the reflectivity coefficient, A is the spacecraft cross section facing the Sun, m is the mass, and $\hat{\mathbf{r}}_{\mathbf{Sun}}$ is the unit vector describing the instantaneous direction of the Sun relative to the spacecraft. To consider a realistic scenario, and introduce the expected perturbation from this source, a reflection coefficient equal to one is assumed for all spacecraft, to simulate a high absorption level from solar panels. Also, it is supposed that the maximum cross section of the satellites is always facing the Sun. The Sun distance and direction are instead derived from the scenario date, and therefore will be realistically similar to the ones of the real mission. When SRP is included in the analysis, $\mathbf{f_s}$ is included in the dynamics Eq. 1, Eq. 2, or Eq. 5, through the term $\mathbf{f_d} = \mathbf{f_s}$.

2.3 Spacecraft's orbits

Hera The Hera trajectory has been selected from the planned hyperbolic passages sequence for the "detailed characterization" mission phase [13]. The selected passage has a pericenter of 10 km and a duration of 4 days, and its direction from Didymos is nearly aligned with the Sun: such a scenario will facilitate image-based navigation thanks to the light reflection from the two CubeSats. The orbit is initialized with a classical Keplerian model, considering the overall mass of the Didymos system. A comparative analysis of different dynamical models (listed in Section 2.2) was carried out. The long distance from the two attractors makes the effect of the moonlet negligible, however, it was observed that SRP contributed a significant disturbance, as shown in Fig. 2. Hence, the final selected trajectory for Hera is defined in the Keplerian model with SRP.

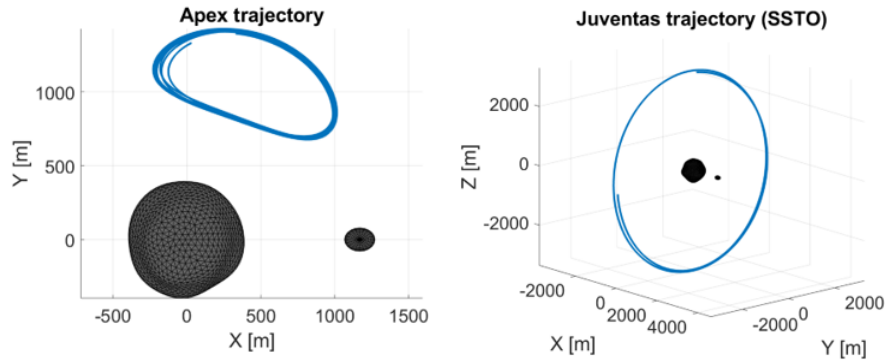

(a) Apex trajectory in the rotating reference frame.

(b) Juventas trajectory in the inertial reference frame.

Fig. 3: CubeSats trajectories.

Apex and Juventas The two CubeSats will be at a much shorter distance from the binary system than Hera, and will be more subjected to the gravitational effect of the two bodies. As anticipated in Section 2.2, the SRP will still play an important role, given the low gravity of the asteroids.

Apex CubeSat will be placed in the surroundings of the Lagrangian point L4 or L5 in the Didymos binary system. Due to the nature of such equilibrium points, the basic dynamics model to be adopted is the CRTBP. The assumed orbit is a Short Period Orbit (SPO) around L4, due to its dimension and stability properties, which make it a good option for spacecraft with limited station-keeping capabilities. The orbital family is computed according to a non-symmetric correction-continuation scheme from the Lagrangian point [19], then the orbit with the best stability properties is extracted from the family. The selected orbit has a period of 12 hours and 20 minutes. The CRTBP orbit is then corrected to the SERTBP, plus the effect of SRP. The final trajectory has a bounded, non-periodic motion, as shown in Fig. 3a.

Juventas CubeSat will be located in a Self Stabilizing Terminator Orbit (SSTO), at a distance between 2 and 5 km from the system's barycenter, and will have an orbital period which is an integer multiple within one week [18]. The present paper assumes a SSTO orbit with a radius of 3.3 km and a period of 56 hours. Because the SSTO orbit is possible uniquely because of the SRP effect, an initial Keplerian model, augmented with SRP, was considered. As for Apex, Juventas's trajectory was corrected in the SERTBP, as shown in Fig. 3b.

2.4 Visibility analysis

Electro-optical sensor characteristics Hera visual sensor and its parameters are essential for the study of a centralized vision-based navigation. The Asteroid Framing Camera (AFC) characteristics of interest are reported in Tab. 1, as from [20]. Such camera model is used to generate realistic synthetic images in PANGU. In operating conditions the AFC is affected by a dark noise with rate $N_{dark} = 0.03$ DN/s

and a read-out noise with standard deviation $N_{read} = 2$ DN. This paper wants to investigate the possibility of exploiting images already taken by Hera for its own navigation. Therefore, images are acquired with a low exposure time $t_{exp} = 0.1$ s, necessary to avoid smear and saturation, since Didymos is the main target [13].

Table 1: AFC characteristics

Parameter	**Value**
Field Of View	FOV = 5.5°
Aperture diameter	$d_a = 20$ mm
Focal length	$f = 150$ mm
Pixels	1024x1024
Bit Depth	$BD = 14$
Analog chain gain	$G = 18$ electrons/DN
Quantum Efficiency (max)	$QE_{max} = 0.2$
Point Spread Function (PSF) diameter	$d_{PSF} = 1.7$ px

CubeSats visibility An analysis is performed to assess when the CubeSats are visible. Four geometric constraints that affect the CubeSats detection are taken into account:

1. the target is in the camera Field Of View (FOV);
2. the target is not overlapped to Didymain or behind the body;
3. the target is not overlapped to Dimorphos or behind the body;
4. the target is not in Didymain or Dimorphos shadow.

Please note that the overlap with a celestial body makes the target impossible to detect because of its small dimension in pixels.

Results are reported in Tab. 2 for both Juventas and Apex. In Fig. 4 and 5 Hera orbit traits are highlighted when the targets are visible. It can be observed that Apex is not visible mainly because it lies on Didymos orbital plane as Hera, therefore it is often covered by Didymain. It is visible in a discontinuous manner. While Juventas is almost always outside the FOV and the trait in which it is visible is unique.

Table 2: CubeSats Visibility

Cubesat	**Contraint**	**Visibility**
Apex	1	35.08 %
Apex	2	78.39 %
Apex	3	100 %
Apex	4	85.58 %
Apex	all	9.17 %
Juventas	1	4.58 %
Juventas	2	100 %
Juventas	3	100 %
Juventas	4	100 %
Juventas	all	4.58 %

From the geometric constraints analysis, it is clear that the overall algorithm performance will be seriously affected by the targets' low visibility and occasional measurements provided by the IP. Such an outcome is highly dependent on the reference hyperbolic arc of Hera. The reference arc is selected based on the trajectory analyzed in [13]. An out-of-plane arc is expected to be beneficial with respect to geometrical constraints mentioned here. Nevertheless, the impact of such constraints on the navigation needs to be evaluated through extensive tests.

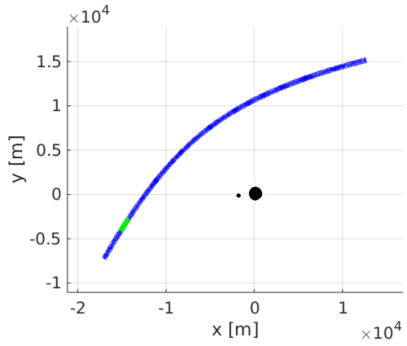

Fig. 4: Juventas visibility during Hera hyperbolic trajectory (green = visible, blue = not visible)

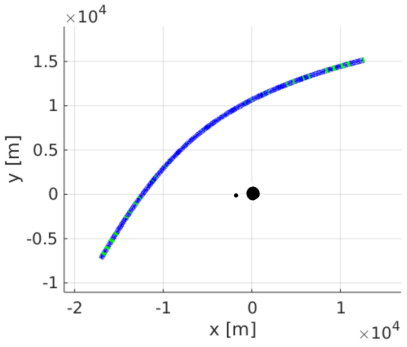

Fig. 5: Apex visibility during Hera hyperbolic trajectory (green = visible, blue = not visible)

3 Image Processing Algorithms/Alternatives

The main sensor considered for the centralized navigation is Hera narrow angle camera. Images can be exploited to derive a LOS measurement for the two CubeSats. In this section, two possible architectures for the IP algorithm are defined, according to the above described mission scenario. Then, they are compared and the baseline is selected and described in detail.

3.1 IP alternatives definition

Depending on the target distance, characteristic dimension and camera characteristics, different IP techniques can be adopted. In Fig. 6, the image portion occupied by the target with characteristic dimension of 60 cm is displayed at different distances for images taken with the AFC. When the CubeSats are close to Hera, feature detection and matching can be used to retrieve the relative pose [28, 29]. Alternatively, the centroid algorithm allows a safe computation of the LOS at distance lower than about 700 km.

Given the ranges in Fig. 7 and Fig. 8, derived from the trajectories in Section 2.3, the CubeSats dimension is always less than the pixel resolution. This poses additional challenges to the CubeSats detection, causing potential false matching

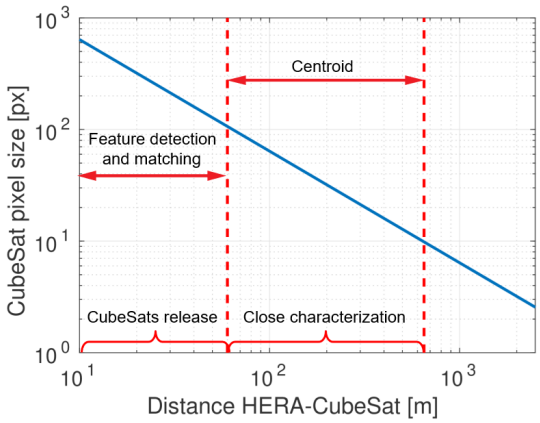

Fig. 6: Image Processing techniques for CubeSats detection

with stars in background or dark current noise. Being the dimension lower than 1 pixel, feature detection and matching is not considered as a valid alternative.

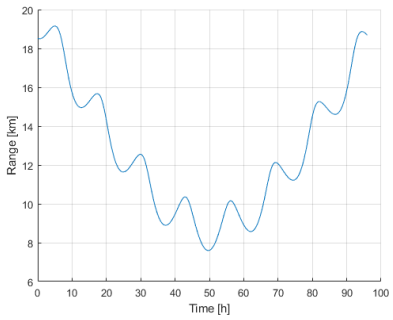

Fig. 7: Range Apex - Hera

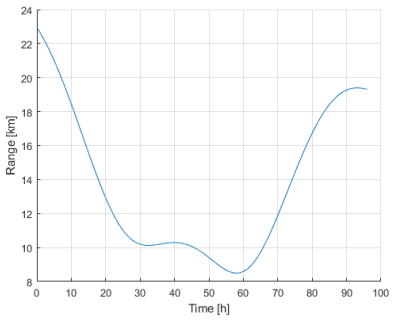

Fig. 8: Range Juventas - Hera

Centroiding is the typical technique used to detect small objects, for instance in star trackers [21]. The *Moment* computation is the simplest and computationally efficient technique, while *Gaussian Fit* can achieve a larger accuracy at the price of a larger computational effort [32]. The *Moment* algorithm is selected in virtue of its simplicity and robustness: considering the low visibility of the CubeSats, the main challenge of the IP is related to false matching avoidance rather than to accuracy in the detection. Moreover, the accuracy obtainable with Gaussian Fit may be limited due to the required threshold choice, especially in cases when the CubeSat and noise sources of error have similar brightness, due to the threshold choice.

Two different general approaches can be adopted for the IP algorithm:

1. the IP assumes *a-priori* information from the navigation filter;
2. the IP does not rely on *a-priori* information from the navigation filter.

Each alternative is analysed in detail in the following sections, making some trade-offs to derive a baseline architecture.

3.1.1 Filter feedback state

No lost-in-space detection is performed: the IP takes as input the CubeSats image coordinates estimated by the filter and their covariance. The IP outputs are the measured targets image coordinates, that are fed into the filter. The IP algorithm is schematized in Fig. 9 and comprises the following steps for each target:

1. **Windowing**. Based on the target estimated position and its uncertainty a window is taken from the image.
2. **Visibility check**. If the window does not respect the visibility constraints, the IP can not detect the CubeSats and the algorithm does not provide a new measurement.
3. **Thresholding**. A threshold is applied to remove background noise and the image is binarized. The threshold should be sufficiently low not to remove the CubeSats pixels and sufficiently high to eliminate background noise.
4. **Clean**. When the target brightness is low, the pixel populations of CubeSat and noise may not be well separated. Isolated pixels are cleaned out of the image.
5. **Centroid**. The centroids associated to the bright pixels are computed. Such points are the possible candidates for the target position.
6. **Candidates screening**. The candidates may be the other target, noise or stars. A screening is performed by checking the two previous sets of candidates. If no past candidates are found in the neighborhood of the new ones, the candidate is discarded. If one and only one candidate remains, the algorithm outputs its coordinates as new measurement.

Please note that the CubeSats are simulated as PSF, given their dimension and the low exposure time. This aspect has been important for the steps selection.

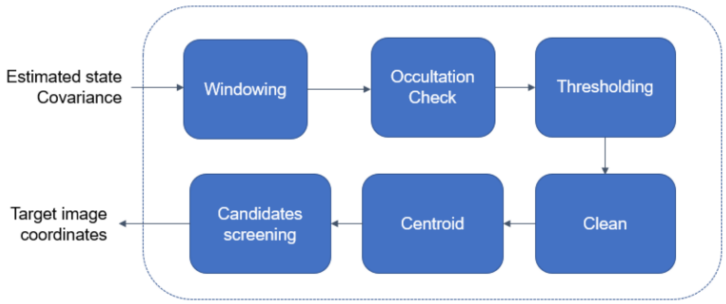

Fig. 9: IP pipeline - filter feedback case

Performance assessment A first performance assessment of the algorithm is performed by simulating simplified synthetic images. The images simulation comprises:

– Gaussian noise;
– PSF, according to CubeSats estimated brightness and AFC characteristics;
– stars background, with stars from SPICE Hipparcos catalog.

Please note that at this stage the IP performance is assessed without including the asteroids in the image.

The IP is tested without the filter in the loop. The filter output is simulated considering a Gaussian distribution with a standard deviation of 100 m on the CubeSats position in the camera frame. Uncertainty propagation is used to derive the window size in the image frame.

Results of the preliminary IP performance assessment are reported in Tab. 3, where the *mean error* between real CubeSats image coordinates and the IP output includes false matching. The percentages are computed with respect to number of frames in which each CubeSat is visible. It can be noticed that the error with respect to real image coordinates is acceptable and that the algorithm never performs a false matching. However, the percentage of cases in which the IP is not able to provide the CubeSat position is still high. The IP algorithm is quite robust in terms of false positives, thanks to the check steps, but this results in a quite high percentage of false negatives.

Table 3: CubeSats Visibility

CubeSat	False Positives	False Negatives	Mean Error
Apex	0.35%	38.5%	1.38 px
Juventas	1.14%	17.8%	1.96 px

3.1.2 No filter feedback

The proposed architecture for the IP algorithm is presented in Fig. 10. The objective of the IP algorithm here is to find the CubeSats in a lost-in-space scenario, where no information comes from the filter. It takes in input two subsequent images and its output is the CubeSats position in image coordinates or a not-found message. Within the image pre-processing block, asteroids are masked and the centroids corresponding to the other celestial and artificial objects is computed; then such points are characterized as features and matched from one image to the other. Finally, disparity is computed and the candidate points are screened.

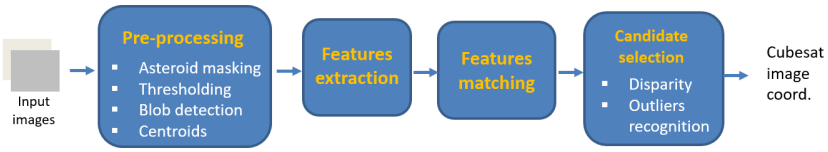

Fig. 10: IP pipeline - no filter feedback case

The blocks are now explained in more detail.

Pre-processing Asteroids in the image are masked, taking into account the uncertainty in Hera pointing. Then, a threshold is applied to remove noise; the image is binarized and cleaned. Finally, stars and CubeSats PSF are detected and their centroid is computed. Such points constitute the pool of candidates.

Features extraction Each candidate needs to be matched with the corresponding one in the previous image. In this process it is essential to have points in the center of highly variable area, which helps in the matching process. Well defined points are found in the presented scenario (i.e. stars, CubeSats), but they are all placed over a background poor of features. Typical features used for stars matching are based on geometric patterns or brightness information. Therefore they are the ones considered here.

Features matching Feature matching is necessary for associating candidate points of the two images and to understand how they moved from one frame to the other. It is possible that a candidate in one image is not visible in the subsequent one; in this case the algorithm shall recognize that the candidate is no longer present in the image.

Candidate selection The disparity of the matched candidates is computed. The stars shall have a similar disparity, as the relative motion between camera and fixed stars is due only to Hera trajectory and pointing. A candidate is selected if its disparity differs significantly from the mean one. The knowledge of CubeSat disparity can be exploited to distinguish among them, since Apex motion is almost planar.

3.2 Comparison and baseline description

3.2.1 Filter feedback vs no filter feedback

The IP architecture trade-off is reported in Tab. 4. The accuracy of the two strategies is similar and the number of false positive (FP) and false negative (FN) are comparable. The first alternative is computationally lighter than the second: simulating one Hera hyperbolic arc, the mean CPU time dedicated to one step of the IP with filter feedback is 0.024 s, while without feedback it is 0.130 s. The simulation has been run on an Intel(R) Core(TM) i7-10510U CPU @ 1.80GHz. The preliminary analyses in the sections above have pointed out that the CubeSats visibility is low, so the IP algorithm measurements provided to the filter are scarce. Hence, in case of assuming preliminary info from the filter, if the filter diverges the IP will not be able to provide any measurement, causing a failure of the navigation architecture. Therefore, in virtue of its robustness, the IP without filter feedback is selected as baseline.

3.2.2 Baseline description

The detailed IP baseline design resulting from the trade-off is shown in Fig. 11.

Table 4: IP main architecture trade-off

Alternative	Accuracy	Robustness	Cost
IP with filter feedback	Medium	Low	Low
IP without filter feedback	Medium	High	Medium

Fig. 11: IP baseline algorithm

Masking The asteroids masking is performed as first step in the image pre-processing. In particular, Didymain position is assumed known from Hera central navigation, while Dimorphos position is not considered known. Dimorphos is assumed on a circular orbit around Didymain, allowing a coarse knowledge of its position. The error in pixels between the two cases is shown in Fig. 12 and can reach about 80 pixels. According to this analysis, to establish the margin, the uncertainty on Dimorphos position is assumed to be equal to the body radius.

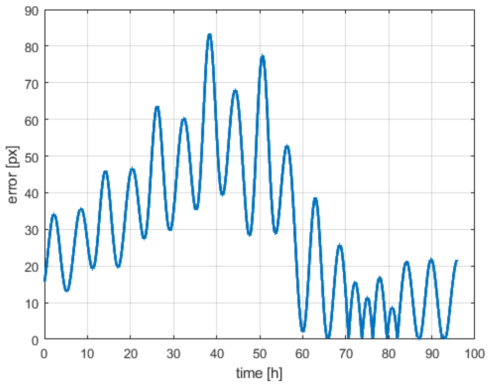

Fig. 12: Error in Dimorphos assumed position, between circular and elliptical orbit.

Threshold and centroids Afterwards, a threshold is applied to the image to remove background noise. The threshold is tuned according to the present scenario.

The result is a binary image where only stars and CubeSats bright enough are visible. Their centroids are computed as center of the detected blobs. Such points constitute the pool of candidates.

Features extraction and matching Each candidate needs to be matched with the corresponding one in the previous image. Triangular features are extracted to associate the stars and CubeSats geometric pattern in the two frames. For each point the two closest ones are considered, forming the three of them a triangle, as shown in Fig 13. Parameters used by Liebe for stars matching are the angles from the star to the closest two neighbours and the inner angle of the triangle [23]. Features are matched with a Sum Squared Differences metric, in order to associate candidate points of the two images and understand how they moved from one frame to the other.

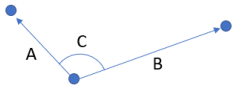

Fig. 13: Triangular Feature A,B,C: A,B = angular distance C = inner angle

Candidate points on the image border Triangular features are identified by searching for the two closest points for each point. When a point appears or disappears in one image, being near to the image border, the pattern can not be correctly matched in the two frames, as the closest points will be different. As an additional check in the candidate selection process, centroids within a few pixels of the image border are removed from the candidate pool, because they are likely not found in subsequent images.

Disparity and outliers identification The disparity of the matched candidates is computed. The stars shall have a similar disparity, as the relative motion between camera and fixed stars is due only to Hera trajectory and pointing. A candidate is selected if its disparity differs from the mean more than a threshold. Such threshold is a number of pixels chosen depending on the image acquisition frequency, given the orbital dynamics scenario. When an outlier is found, it is removed and other outliers are searched for with an iterative procedure.

Distinguish Apex and Juventas Once candidates have been screened and outliers found, it is necessary to distinguish between Apex and Juventas. The criteria used are the following:

1. a candidate is recognized as Apex if its disparity, which has a direction similar to the CubeSat velocity, is mainly horizontal and if the CubeSat is close to the asteroid plane;
2. a candidate is recognized as Juventas if it is not Apex and its velocity is mainly vertical, as it should be during visibility periods from the scenario preliminary analysis.

Table 5: List of *FIL* requirements for the tool implementation

ID	Requirement
FIL-1	The filter shall implement a centralized solution for relative navigation.
FIL-2	The filter shall process measurements from two cubesats.
FIL-3	The filter shall process IP and another source of relative measurement.
FIL-4	The filter shall use as input the estimated trajectory of Hera.
FIL-5	The filter shall be executable on-board.

4 State Estimation Algorithm

The peculiar dynamics and nonlinear measurements for the CubeSats state in the reference scenario requires an efficient and effective nonlinear state estimation algorithm. In this paper, the Extended Kalman Filter (EKF) has been selected for the implementation. Major trade-offs concerned the dynamics of the system and the formulation of the EKF. In this section the alternatives are presented and compared. The baseline architecture for the study is summarized. The major filter requirements (*FIL*) that drove the algorithm design are reported in Tab. 5.

4.1 Filter architecture

The two most-used and best performing filtering techniques in presence of nonlinear dynamics or measurements are the extensions of the Kalman Filter. In particular the Extended Kalman Filter (EKF) and the Unscented Kalman Filter (UKF) are assessed and compared in terms of navigation accuracy and computational burden. In general, the UKF does not necessarily provide much better results compared to EKF. It depends on the state uncertainties and the nonlinearity of the dynamics and measurement models. Nevertheless, for angles-only navigation-like problems the UKF has shown slightly better results in terms of average location accuracy and consistency of the estimates, as reported in [16]. In order to deal with uncertain parameters, unobservable or whose dynamics is unknown, the Schmidt formulation is evaluated.

Table 6: Filter techniques trade-off.

Model	Accuracy	Robustness	Cost
EKF	Medium	Medium	Low
UKF	High	Medium	High
Schmidt-EKF	Medium	High	Low
Schmidt-UKF	High	High	High

From the trade-off, both the EKF and UKF techniques, using Schmidt formulation are promising candidates. One of the drawbacks of of UKF is the high computation demand. Nevertheless, this may not be a dramatic issue given the navigation sample time in this application (60 s). Despite these considerations, the Schmidt-EKF is selected as baseline for its reduced computational burden,

respecting *FIL* requirements. The Schmidt-UKF is a valid alternative, in case the EKF fails in reconstructing the dynamics with acceptable accuracy. Future works may focus on implementing the UKF alternative to deal with the non-linearities of the measurement function. Additionally, a hybrid solution can be investigated to guarantee accuracy limiting the computational costs.

4.2 Dynamical model and Reference Frame

One important building block of the filter algorithm is the dynamical model to adopt in the state prediction step. The scenario is around a binary system, where two gravitational bodies are present. The trade-off has been performed between the Restricted Three Body Problem, the Perturbed Two-Body Problem (PTBP) and the Circular Restricted Three Body Problem (CRTBP).

Table 7: Filter dynamical propagation trade-off.

Model	**Reference Frame**	**Accuracy**	**Cost**
PTBP	Inertial	Medium	Low
RTBP	Inertial	High	Low
CRTBP	Synodic	High	Low

The CubeSats orbits described in Section 2 are peculiar of the three-body problem environment, see for instance Apex trajectory. Moreover, being in close proximity to Dimorphos, a comprehensive description of the gravitational pull of the primaries is needed. The computational cost to perform the state propagation is comparable and limited, hence the CRTBP and the RTBP have been chosen for implementation. The two dynamical models refer to the same gravitational scenario. The trade-off shifts to the selection of the most appropriate reference frame to use. In the case Dimorphos ephemeris are not known, the CRTBP expressed in the synodic frame is suggested to include secondary asteroid motion in the equations. Nevertheless, in this study the Hera trajectory is reconstructed in the inertial reference frame centered at the primary [17]. Thus, it is convenient to express the dynamics of the CubeSats into the same reference frame. Such strategy prevents the measurement equation from being affected by dynamics parameters, such as the angular velocity of the system. In this way, the dynamical propagation and the measurement update are not correlated. For this reason the RTBP, expressed in the inertial frame centered in Didymain and assuming circular motion of the secondary, is chosen for implementation.

4.3 Estimation algorithm: baseline description

In order to obtain a fully-observable solution from the low observability of the sensor measurements in the presence of large dynamics uncertainties and measurements non-linearities the filter design relies on the non-linear extension of the Kalman filter. In particular, the Schmidt-EKF is selected as baseline in this paper.

4.3.1 Filter dynamical propagation

The augmented state vector $\mathbf{X}$ can be decomposed into *solved-for* S and *considered* C states:

$$\mathbf{S} = ([\mathbf{r}_i, \mathbf{v}_i], \mathbf{X}_H^T, \mathbf{a}_{dyn})^T, \ \mathbf{X}_H = (\mathbf{r}_H, \mathbf{v}_H)^T \ \ \forall i \ \ \text{SC} \qquad \mathbf{C} = (\mu_p, \mu_s, b_\rho)^T \quad (15)$$

where $(\mathbf{r}, \mathbf{v})^\mathbf{T} = (x, y, z, \dot{x}, \dot{y}, \dot{z})^T$ are position and velocity vector in the inertial frame centered at the primary asteroid, $\mathbf{X}_H = (\mathbf{r}_H, \mathbf{v}_H)^T$ represents the state vector of Hera main spacecraft with respect to the same reference frame, $\mathbf{a}_{dyn}$ is the unmodelled acceleration disturbance in the elliptical three body problem acting on both CubeSats, μ_p and μ_s are the gravitational parameters of the Didymos system and b_ρ is the ranging measurement bias. In this formulation it is assumed that Dimorphos ephemeris are available. In case this is not true, an additional state $(\mathbf{r}_s, \mathbf{v}_s)^T$ can be included as *solved-for*. The dynamical propagation of the *solved-for* states in the filter is performed using the restricted three body problem formulation (RTBP) centered at the primary asteroid (the secondary gravitation represents a third body perturbation [17]):

$$\dot{\mathbf{S}} = \begin{cases} \mathbf{v} \\ -\mu_p \frac{\mathbf{r}_i}{r_i^3} - \mu_s \frac{\mathbf{r}-\mathbf{r_s}}{\|\mathbf{r}-\mathbf{r_s}\|^3} - \mu_s \frac{\mathbf{r_s}}{\mathbf{r_s^3}} + \mathbf{a}_{dyn}, \quad \forall i \ \ \text{SC} \\ \mathbf{v}_H \\ -\mu_p \frac{\mathbf{r}_H}{\mathbf{r}_H^3} \\ -\frac{\mathbf{a}_{dyn}}{\tau} \end{cases} \quad (16)$$

where $\mathbf{r_s}$ is the secondary asteroid position vector. The acceleration bias $\mathbf{a}_{dyn}$ is modelled as an exponentially correlated random variable (first-order Gauss-Markov process) for dynamic model compensation. The time constant τ gives the correlation time, which can be thought as the time over which the intensity of the time correlation will fade to e^{-1} of its prior value. Hera state is assumed to be known, meaning that no IP measurement processing of the main Hera spacecraft is required to retrieve its full state. CubeSats navigation receives the processed estimate by the Hera navigation. Moreover, the initial covariance is known but it is not foreseen that the Hera state covariance is fed to the CubeSats navigation at each step. This is done to reduce the impact of implementing the proposed centralized navigation in the consolidated GNC system of the main spacecraft. For this reason and to enhance the robustness of the filter, the filter includes it in the *solved-for* augmented state. The a-priori estimate is generated using Keplerian motion around the primary asteroid to reduce computational load. Synthetic measurement of the full state will then be included in the measurement update. In this formulation it is assumed that Dimorphos ephemeris are available. In case this is not true, the additional state $(\mathbf{r}_s, \mathbf{v}_s)^T$ dynamics can be assumed as Keplerian motion. Initialization of Dimorphos position is needed. The *considered* states are assumed to be uncertain parameters with no process noise dynamics. Hence:

$$\dot{\mathbf{C}} = \mathbf{0} \quad (17)$$

In order to fully develop the EKF estimation algorithm, the linear matrices concerning the Jacobian and State-Transition-Matrix (STM) are required. The Jacobian is referred with the matrix $\mathbf{A}(t)$. The STM is defined as in Eq. 18, where $\mathbf{S}$

is the *solved-for* state vector:

$$\boldsymbol{\Phi}(t, t_0) = \frac{\partial \underline{S}(t)}{\partial \underline{S}(0)} \tag{18}$$

The STM is the result of the integration described in Eq. 19:

$$\boldsymbol{\Phi}(t, t_0) = \int_{t_0}^{t} \dot{\boldsymbol{\Phi}}(\tau, t_0) d\tau \tag{19}$$

where

$$\begin{cases} \dot{\boldsymbol{\Phi}}(t, t_0) = \mathbf{A}(t)\, \boldsymbol{\Phi}(t, t_0) \\ \boldsymbol{\Phi}(t_0, t_0) = \mathbf{I}_3 \end{cases} \tag{20}$$

The integration of the STM can be replaced by a series approximation according to Tab. 8.

Table 8: STM approximations

Method	**Expression**
1^{st}-order Taylor	$\mathbf{I} + \mathbf{A}_t \Delta t$
2^{nd}-order Taylor	$\mathbf{I} + \mathbf{A}_t \Delta t + \mathbf{A}_t^2 \frac{\Delta t^2}{2}$
2^{nd}-order Taylor, no $\dot{\mathbf{A}}$	$\mathbf{I} + \mathbf{A}_t \Delta t + (\dot{\mathbf{A}} + \mathbf{A}_t^2) \frac{\Delta t^2}{2}$

The integration in Eq. 19 can be carried out on-board. Nevertheless, implementation tests need to determine the gain in accuracy at the cost of computational cost to consider the integration beneficial with respect to the approximation. Also, such trade-off is strongly dependent on the navigation sample time, which is set to 60 s in this study. The UKF does not rely on the analytical formulation of the Jacobian matrix of both the dynamics and the measurement model. Indeed, UKF replaces first-order truncation of Taylor series approximations with second-order numerical differencing equations to approximate nonlinear dynamics and measurement models.

4.3.2 Measurement function

The visual navigation camera is the main source of measurements. The measurements are the line-of-sight unit vector coupled with an additional relative Inter-Satellite Link ranging. The frequency of the navigation is dependent on the image availability, hence, in this study, the navigation frequency is set to $\frac{1}{60}$ Hz. The

Table 9: Types of measurements for centralized relative navigation

Sensor	**Measurement**
Camera	Eq. 21
Ranging	$\|\mathbf{r}\|$
Central Nav.	$\mathbf{X}_H^{1:6}$ (synthetic)

sensor suite and measurements potentially employable are summarized in Tab. 9. In addition, the ephemeris of Hera delivered by the mothercraft navigation are treated as synthetic measurements. This is done in order to preserve covariance of the estimation coming from the main Hera navigation system.

Camera The measurement model for the optical measurement is developed here, based on the well established pinhole camera model. The IP algorithm yields the homographic coordinates of the relative position, denoted with $\boldsymbol{\rho}$ of the CubeSats with respect to the mothercraft.

$$\mathbf{Y}_c = \boldsymbol{\rho}_h = \begin{bmatrix} \mathbf{x}_h \\ \mathbf{y}_h \end{bmatrix}_{\boldsymbol{\rho}} \Longleftrightarrow \boldsymbol{\rho}_c = \begin{bmatrix} \mathbf{x}_c \\ \mathbf{y}_c \\ \mathbf{z}_c \end{bmatrix}_{\boldsymbol{\rho}} = -\boldsymbol{R}_I^c \frac{\boldsymbol{\rho}}{\|\boldsymbol{\rho}\|} = -\boldsymbol{R}_I^c \frac{\mathbf{S}^{1:3} - \mathbf{X}_H^{1:3}}{\|\mathbf{S}^{1:3} - \mathbf{X}_H^{1:3}\|} \tag{21}$$

where $\mathbf{Y}_c$ is the filter measurement vector partition relevant to the optical measurement. It is noted that the state of the CubeSats are decoupled, moreover the state vector $\mathbf{X}_H$ is part of the augmented state vector. The subscript denotes the reference vector expressed in the different reference frames. The matrix $\mathbf{R}_I^c$ is the rotation matrix from the inertial frame to the camera frame. The exact derivation can be used to express all variables in the inertial frame. The formulation presented here is completely decoupled from the dynamics, being the state expressed in the same reference frame.

Ranging The ranging measurements provide the magnitude of the relative distance between the CubeSats and the main spacecraft, according to Eq. 22:

$$\mathbf{Y}_r = \|\boldsymbol{\rho}\| = \|\mathbf{S}^{1:3} - \mathbf{X}_H^{1:3}\| \tag{22}$$

The range measurements can be achieved by using RF inter-satellite architecture. In general the range error model through RF can be expressed:

$$e_\rho = b_\rho + v_\rho \tag{23}$$

where b_ρ is representative of the biases and v_ρ of a random white noise $v_\rho \sim \mathcal{N}(0, \sigma_\rho)$. The bias term, when dealing with RF-systems, derives from different sources such as antenna offset, light time delay, clock synchronization (one-way ranging). In the case of Two-Way Ranging (TWR), hereby suggested for implementation, no synchronization is needed between the clocks of the two spacecrafts. However, the dynamics of these measurement biases cannot be accurately modeled, so the resulting estimates may include uncertain values. In the Schmidt formulation measurement biases can be mitigated by augmenting the classical Kalman filter and then discarding the update equations of the measurement biases [24]. The measurement biases can potentially be modeled as a random constant vector with the *a-priori* known statistics, which are assumed to be independent of the true state evolution. In the hypothesis of assuming the rest of the errors and biases can be eliminated with a good calibration, the error modelling for the ranging measurements reduces to a white noise model.
The full measurement vector is $\mathbf{Y} = [\mathbf{Y}_r, \mathbf{Y}_c]^T$ (or $\mathbf{Y} = [\mathbf{Y}_d, \mathbf{Y}_c]^T$) and the measurement function is defined as $\mathbf{Y} = h(\mathbf{X})$.

4.3.3 Measurement Check

The IP measurement is checked before being processed by the filter. The Mahalanobis distance is used as measurement check metric.

$$M_k = \sqrt{(\mathbf{Y}_k - h(\mathbf{X}_k^-))^T (\mathbf{P}_k^-)^{-1} (\mathbf{Y}_k - h(\mathbf{X}_k^-))} \tag{24}$$

Covariance Check The simplest check for IP measurement consists on comparing the *a-priori* line-of-sight prediction with the actual measurement. Following [17], in case the Mahalanobis distance of the *a-priori* LOS to the LOS provided by the IP is larger than 5 sigma, the measurement delivered by the IP is rejected.

Null-hypothesis Check It is assumed that the observation is Gaussian distributed with mean and variance and associated probability density function. If this does not hold, for instance there are some outliers in the observation or that the Gaussian distribution of the observation noise is influences with some other distributions, the normal probability density function no longer holds. Dedicated hypotheses test can be carried out to detect the modeling errors. In particular, the purpose of performing the null-hypothesis test is to check whether the actual measurement is compatible with the assumed model, i.e. null-hypothesis. As reported in [8], the judging index can be set to the square of the Mahalanobis distance:

$$\gamma_k = M_k^2 \tag{25}$$

Assuming the null-hypothesis is true, γ_k should be Chi-square distributed with degree of freedom 2. We can set a significance level α, which represents a probability threshold below which the null hypothesis will be rejected, is selected. α is typically a small value. The α-quantile χ_α of the Chi-square distribution is predetermined for a given α. In this way we have:

$$\mathcal{P}(\gamma_k > \chi_\alpha) = \alpha \tag{26}$$

which states that the probability of a randomly picked γ_k (not yet evaluated for the actual measurement $\mathbf{Y}_k$) being larger than χ_α should be equal to α. Then, evaluating the judging index γ_k for the actual measurement $\mathbf{Y}_k$, we can check whether γ_k¿χ_α. If this occurs, the null-hypotheses can be rejected and it can be concluded that there exist some kind of violations to the basic assumptions, such as the presence of outliers.

4.3.4 Filter scheme

The Schmidt-EKF filter is here reported in Algorithm 1 as baseline design for the filtering technique. The dynamics and the measurement model are those described in the previous section. It is important to stress that the *considered* parameters are not updated.

The function f embodies the RTBP formulation and the null-dynamics of the *considered* states. $\mathbf{Q}$ is the process covariance matrix, whereas $\mathbf{R}$ is the measurement covariance matrix. The architecture resembles the standard EKF scheme, with the exception of the *posterior covariance update*. The *Joseph's Formula* is employed for stability reasons [7]. In the Schmidt-Kalman formulation the state update is null for the *considered* states and the gain matrices are reshaped accordingly.

Algorithm 1 Centralized EKF

1: $\hat{\mathbf{X}}_k^- = \int_{t_{k-1}}^{t_k} f(\mathbf{X}(\tau))d\tau, \quad \mathbf{X}_{k-1} = \hat{\mathbf{X}}_{k-1}, \quad \hat{\mathbf{X}}_0^+ = \mathbf{X}_0$
2: $\mathbf{A}_k = \frac{\partial f}{\partial \mathbf{X}}\Big|_{\hat{\mathbf{X}}_{\mathbf{k-1}}}, \mathbf{H}_k = \frac{\partial h}{\partial \mathbf{X}}\Big|_{\hat{\mathbf{X}}_{\mathbf{k}}^-}$
3: $\mathbf{P}_k^- = \boldsymbol{\Phi}(t_k, t_{k-1})\mathbf{P}_{k-1}^+\boldsymbol{\Phi}^T(t_k, t_{k-1}) + \mathbf{Q}, \quad \mathbf{P}_0^+ = \mathbf{P}_0$
4: $\mathbf{K}_k = \mathbf{P}_k^-\mathbf{H}_k^T(\mathbf{H}_k\mathbf{P}_k^-\mathbf{H}_k^T + \mathbf{R}_k)^{-1}$
5: $\hat{\mathbf{X}}_k^+ = \hat{\mathbf{X}}_k^- + \mathbf{K}_k(\mathbf{Y}_k - h(\mathbf{X}_k^-))$
6: $\mathbf{P}_k^+ = (\mathbf{I} - \mathbf{K}_k\mathbf{H}_k)\mathbf{P}_k^-(\mathbf{I} - \mathbf{K}_k\mathbf{H}_k)^T + \mathbf{K}_k\mathbf{R}\mathbf{K}_k^T$

5 Numerical Results

The vision-based navigation algorithm has been evaluated in the reference scenario. Representative images have been synthetically generated using PANGU, including the binary asteroid system and the CubeSats, based on the reference built trajectories. An example of generated image is shown in Fig. 14.

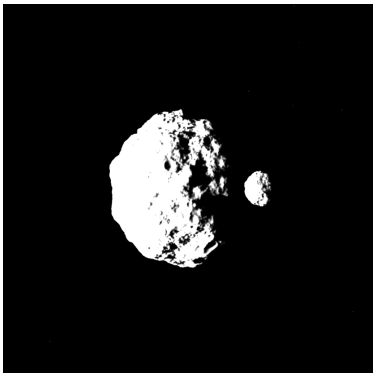

Fig. 14: Example of synthetic image of Didymos system, stars and CubeSats, generated in PANGU considering the AFC model.

The ranging measurements are derived from the relative *true* position and the reference statistics and bias. The image processing block output is fed to the estimation algorithm, which solves for the states. The true concern of this study is the lack of visibility and consequently of LOS measurements during Hera passage. For this reason, the tests were divided into validation of the single blocks, namely IP and filter, before simulating the reference scenario. The architecture for testing is shown in Fig. 15.

5.1 IP results

The IP algorithm is run for the whole trajectory, using images from PANGU. Results of measurements coming from the algorithm are presented in Tab. 10. In particular, a match is considered correct if the error between nominal and measured position is < 10 pixels for Apex and < 15 pixels for Juventas. Otherwise, the point

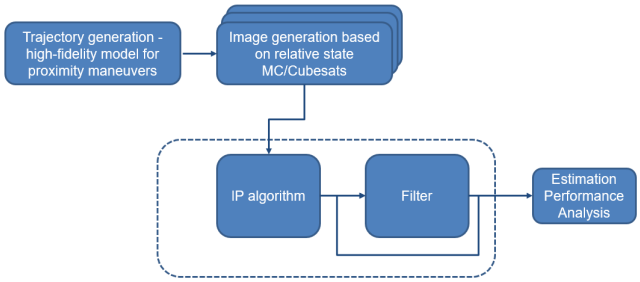

Fig. 15: Navigation scheme used for the algorithm numerical validation.

is considered to be a FP. The number of FN is deduced from the visibility analysis. The IP is able to detect the CubeSats and correctly distinguish them from stars, background noise and among them, notwithstanding their limited visibility and the presence of other objects in the scene (Didymain and Dimorphos). The number of FP is kept low, avoiding to provide incorrect measurements to the filter. Please note that the high number of FN is due to asteroids masking and especially to Dimorphos, for which the masking margin is 1.5.

Table 10: IP performance.

	Visible	**Correct Matches**	**FP**	**FN**	**Error μ** $[px]$	**Error σ** $[px]$
Apex	535	425	14	110	4.85	1.68
Juventas	269	209	12	60	7.93	2.29

The IP measurement error model is shown in Fig. 16 for Apex measurements and in Fig. 17 for Juventas. The error is the difference between the measured pixel coordinates and the pixel coordinates that would be obtained with a perfect imaging system (i.e. no PSF, no distortion). It can be seen that the error differs

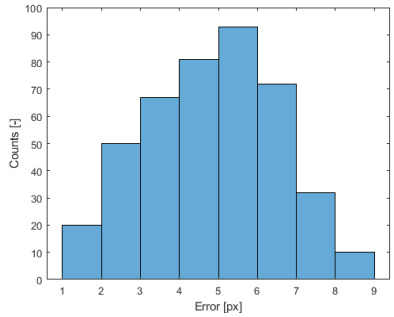

Fig. 16: Apex measurements error

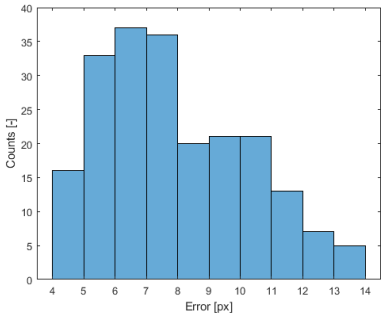

Fig. 17: Juventas measurements error

for the two CubeSats. This may be due to different reasons, here listed:

- Juventas when visible is close to the image border, where the camera distortion is stronger and therefore the error in the measured position is larger;
- the different distance and therefore brightness of the CubeSats can cause a different PSF intensity distribution. The threshold therefore affects differently the PSF areas and if the kept area is larger, the error may be larger as well.

5.2 Open-loop reference scenario

The full-chain algorithm has been tested for the reference scenario. As stated, the major challenge is to cope with the lack of visibility. In particular, without LOS measurements, the filter must rely on the dynamical propagation, and on the nearly-continuous ranging. Both the dynamics and the continuous ranging present drawbacks:

- The dynamical model is kept simple for light implementation on-board. Perturbations, such as solar radiation pressure, irregular masses or elliptical motion, are not implemented. The state variable a_{dyn} was purposely selected to estimate such unmodelled terms and aid the *a-priori* estimate. Nevertheless, the highly non-linear environment requires good initialization of the estimated state to deliver an acceptable state prediction. This is not always guaranteed due to the intrinsic estimation error of the algorithm.
- The nearly continuous ranging is a scalar measurement. When dealing with range-only measurements, the system becomes unobservable and the measurements Jacobian spreads the covariance on all the states involving the CubeSats and Hera spacecraft. As reported in Tab. 11 the estimation of Apex orbit is enhanced when taking into account a continuous ranging measurement, whereas Juventas estimation diverges in the same settings. This may be due to the geometry of the orbits of Hera, Apex and Juventas shown in Fig. 18 together with the camera pointing vector. Juventas moves on a plane perpendicular to the camera pointing direction nearly-symmetric with respect to the hyperbolic passage of Hera. The period of the orbit is larger than Apex's one, thus the ranging does not capture the full harmonic variation as shown in Fig. 8. On the other hand, Apex moves on quasi-parallel plane with respect to Hera's orbit one, making the ranging variations more significant and meaningful. Moreover, one possible justification is that non-Keplerian orbits are peculiar in shape, reducing the ambiguity of the reconstruction from a ranging trend with respect to nearly-Keplerian ones, such as Juventas orbit. Finally, Apex visibility is larger than Juventas, hence the results on the impact of continuous ranging are biased by such phenomenon.

In this regime, the tuning of the filter is critical to find the correct process covariance matrix and state covariance initialization. The Schmidt-Kalman formulation improves the estimation, retaining the uncertainties on dynamical parameters. The parameters used in the simulations are reported in Tab. 11. Hera trajectory is assumed to be known from the central navigation. The reference trajectory is perturbed with Gaussian noise with $\sigma_H = 100\ m$ [17]. The ranging measurements are generated in the same fashion: the ranging yielded by the reference trajectory

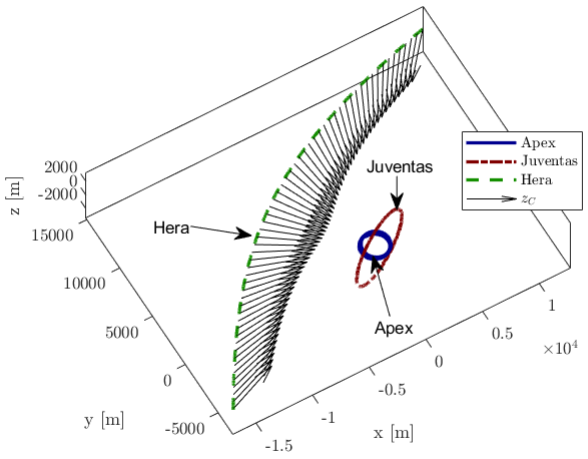

Fig. 18: Trajectories of the spacecrafts (Hera, Apex and Juventas) in the reference scenario. All the trajectories are plotted in the inertial frame.

Table 11: Simulation settings and results in the nominal scenario.

Parameter	**Range**	**Units**
$\mathbf{P}_{0,r}$	$[10^1]^2 \cdot \mathbf{I}_{3\times3}$	m^2
$\mathbf{P}_{0,v}$	$[10^{-3}]^2 \cdot \mathbf{I}_{3\times3}$	$\frac{m^2}{s^2}$
$\mathbf{P}_{0,r_H}$	$[10^2]^2 \cdot \mathbf{I}_{3\times3}$	m^2
$\mathbf{P}_{0,v_H}$	$[10^{-1}]^2 \cdot \mathbf{I}_{3\times3}$	$\frac{m^2}{s^2}$
$\mathbf{P}_{0,a_{dyn}}$	$[10^{-9}]^2 \cdot \mathbf{I}_{3\times3}$	$\frac{m^2}{s^4}$
$\mathbf{Q}_r$	$[10^1]^2 \cdot \mathbf{I}_{3\times3}$	m^2
$\mathbf{Q}_v$	$[10^{-2}]^2 \cdot \mathbf{I}_{3\times3}$	$\frac{m^2}{s^2}$
$\mathbf{Q}_{r_H}$	$[10^2]^2 \cdot \mathbf{I}_{3\times3}$	m^2
$\mathbf{Q}_{v_H}$	$[10^{-1}]^2 \cdot \mathbf{I}_{3\times3}$	$\frac{m^2}{s^2}$
$\mathbf{Q}_{a_{dyn}}$	$[10^{-7}]^2 \cdot \mathbf{I}_{3\times3}$	$\frac{m^2}{s^4}$
$\mathbf{a}_{dyn,0}$	10^{-7}	$\frac{m}{s^2}$
τ	10^4	s

	Value	**Units**
RMS ρ_{Apx}	32.61	m
RMS v_{Apx}	0.01	$\frac{m}{s}$
RMS ρ_{Jvt}	242.52	m
RMS v_{Jvt}	0.01	$\frac{m}{s}$

was perturbed with a Gaussian noise with $\sigma_r = 1\ m$ and bias $b = 10\ m$. The estimated bias term is set to 0 m. The centralized autonomous navigation delivers the estimation results summarized in Tab. 11. The lack of LOS measurements is challenging for the filter, especially in such dynamics domain. As already stated, the ranging measurements are beneficial for Apex orbit reconstruction, whereas they lead to instability and divergence when inserted in Juventas estimation. Fig. 20 shows the position estimation results for Apex nominal scenario simulation. Fig. 20 the estimated trajectory compared to the reference one. Fig. 20 shows how the lack of LOS measurements affect the estimation by leading to maximum Root-Mean-Squared error (RMS). When LOS measurements are not available, the filter

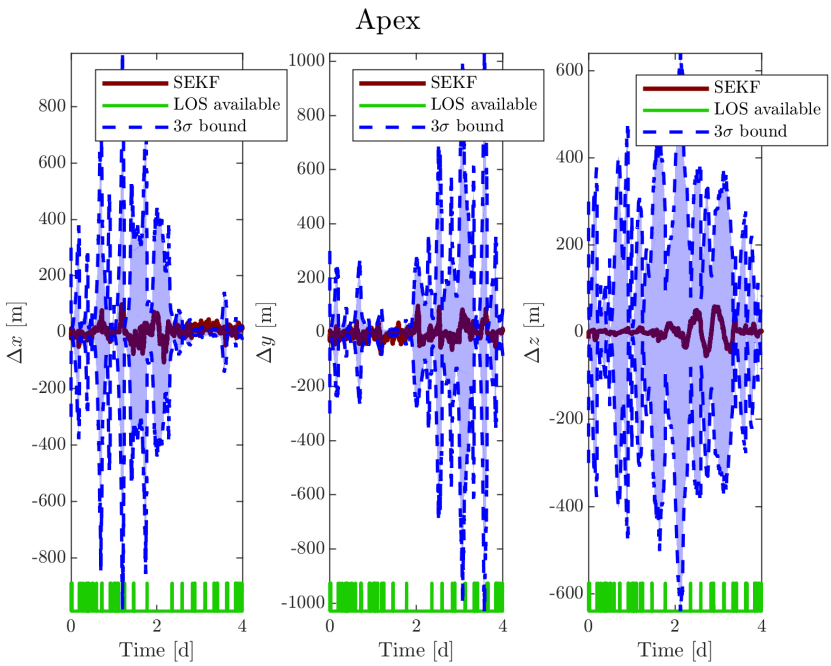

Fig. 19: Apex position error in x, y, z axis component in inertial frame. The estimated covariance drops when LOS measurement becomes available.

relies on dynamics and ranging, starting the *a-priori* estimation from the last estimated state. Given that the orbit exists in non-Keplerian dynamics, the initial condition for dynamical propagation is fundamental. The filter covariance matrix enlarges enough in order to pass through the measurement check and accept the LOS measurement as valid even if the estimation is far off from *true* value. The Schmidt-Kalman formulation improves the estimation by keeping the uncertainty on the dynamics and bias parameters. Fig. 22 shows the position estimation results for Juventas nominal scenario simulation, along with the estimated trajectory compared to the reference one.

Juventas visibility is critical, exploiting solely a narrow window for LOS measurements. The Schmidt-Kalman formulation prevents the filter from diverging and delivers a lower estimation error, as shown in Fig. 22. The results for the centralized autonomous navigation shows that the estimation is possible if the values for the RMS in Tab. 11 are acceptable. The nominal scenario refers to a particular hyperbolic passage [13] assuming the navigation camera always points towards the asteroid for central navigation purposes.

5.3 Maximum *Blind Time* Assessment

The open-loop scenario simulated using a tuned filter demonstrated that the most critical aspect of the autonomous centralized navigation is the lack of optical mea-

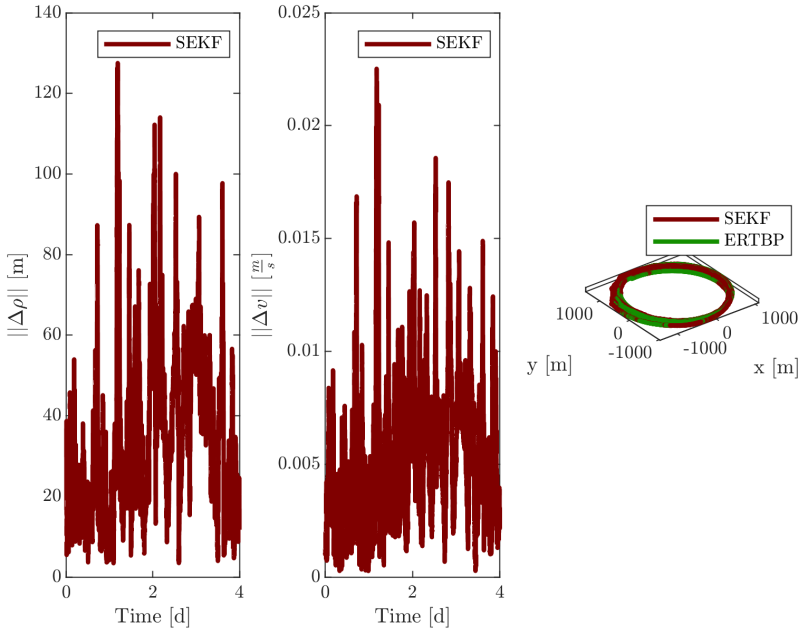

Fig. 20: Position and velocity error for Apex estimation and estimated orbit shown in the inertial reference frame.

surements. Indeed, even though the achieved accuracy is considered acceptable for the CubeSat operations, the estimation error is quite large to effectively reconstruct the trajectories of the cubesats. For this reason, a Monte Carlo approach would be useless, being the robustness critical point already identified. In order to assess the suitability of the presented architecture for the autonomous centralized navigation of the CubeSats, an additional analysis has been performed to assess the achievable navigation accuracy as a function of LOS *blind time*. In particular, the estimation accuracy as a function of the *blind time* has been explored. The analysis is based on variable time frequency of a fixed measuring window, comprising 10 measurements. Basically, the hyperbolic passage duration is taken as full scale and the measuring frequency is spanned from no measurements to continuous ones. Fig. 23 reports the results for the estimation accuracy as a function of the measurement frequency. Fig. 23 shows that the estimation accuracy exponentially improves as the measurements frequency increases. For instance, this means that even with 10 measurements batches per day the position estimation error never inflates more than 90 m. Filter settings are kept equal to the open-loop nominal simulation.

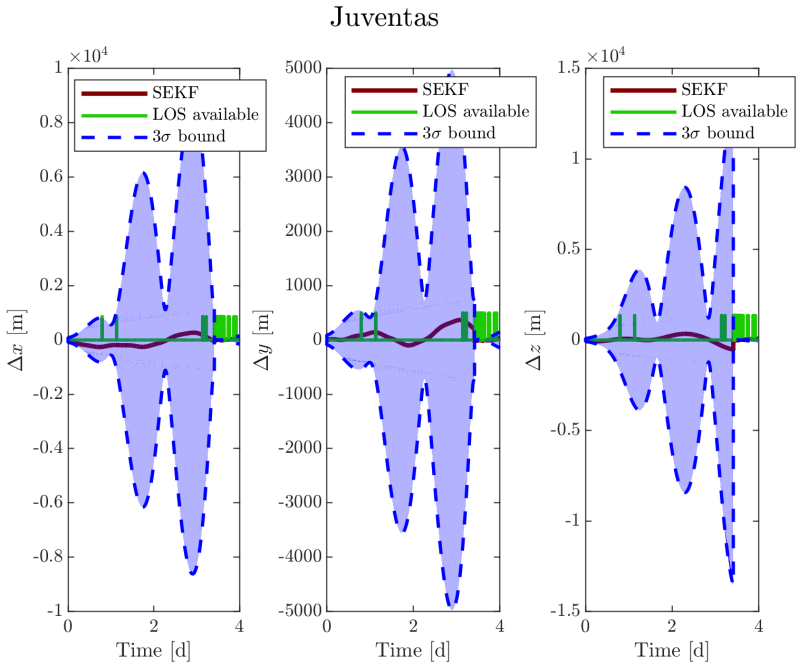

Fig. 21: Juventas position error in x, y, z axis component in inertial frame. The LOS availability is shown. The estimated covariance is propagated when no measurements are fed to the filter. Consequently, it significantly reduces once the visibility is restored at the end of the trajectory.

6 Conclusion

A centralized autonomous relative navigation architecture is proposed for proximity operations of the CubeSats in Hera mission. The navigation of Apex and Juventas CubeSats during proximity operations is challenging due to the nature of the dynamics and the constrained visibility. The reference trajectories are generated using a high-fidelity model, including irregular shapes and non-Keplerian environment. A visibility analysis has been conducted to identify the constraints and limitations in LOS measurements during the hyperbolic passage of Hera spacecraft. The image processing algorithm is a centroid identification, which is able to detect the CubeSats using asteroid masking, feature extraction/matching and a final disparity analysis. The algorithm performance model has been derived. An Extended Kalman Filter, implemented following the Schmidt formulation, with 21 *solved-for* states and 3 *considered* is able to deliver an estimation error in the order of $\sim 10^2$ m for both CubeSats. When LOS measurement are not available, the ranging-only navigation degrades the estimation of Juventas trajectory, whereas it is beneficial for Apex. The results for the centralized autonomous navigation show that the estimation is possible if the resulting RMS errors are acceptable. The nominal scenario refers to a particular hyperbolic passage assuming the navigation

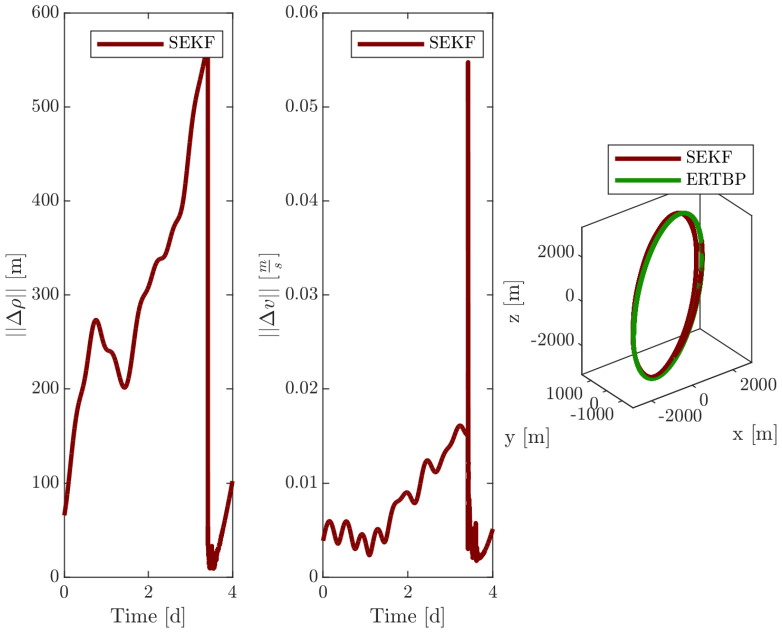

Fig. 22: Position and velocity error for Juventas estimation and estimated orbit shown in the inertial reference frame.

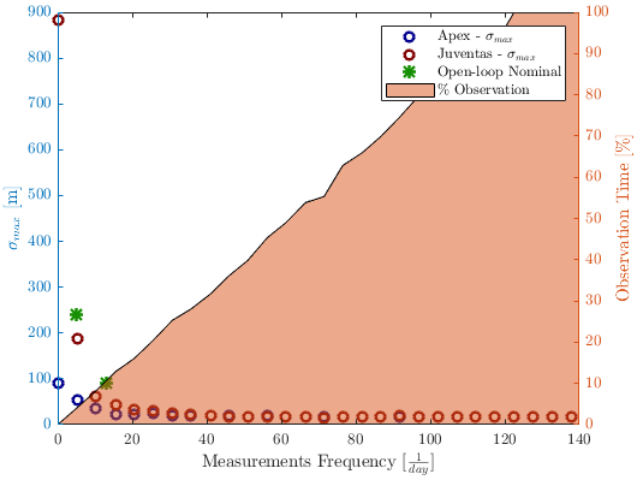

Fig. 23: Estimation accuracy as a function of measurements frequency.

camera always points the asteroid for central navigation purposes. A maximum *blind-time* analysis has shown that a periodic pointing towards the CubeSat would dramatically enhance the relative orbit estimation, with a lower RMS error. Future tests will focus on tuning optimally the filter by using a statistical approach.

Acknowledgements The presented work was carried out under ESA funding ESA RFP/3-16012/19/NL/CRS/hh, item no. 19.3EC.04.

Conflict of interest

On behalf of all authors, the corresponding author states that there is no conflict of interest.

References

1. Adams, E., O'Shaughnessy, D., Reinhart, M., John, J., Congdon, E., Gallagher, D., Abel, E., Atchison, J., Fletcher, Z., Chen, M., et al.: Double asteroid redirection test: The earth strikes back. In: 2019 IEEE Aerospace Conference, pp. 1–11. IEEE (2019)
2. Balmino, G.: Gravitational potential harmonics from the shape of an homogeneous body. Celestial Mechanics and Dynamical Astronomy **60**(3), 331–364 (1994)
3. Capannolo, A., Ferrari, F., Lavagna, M.: Families of bounded orbits near binary asteroid 65803 didymos. Journal of Guidance, Control, and Dynamics **42**(1), 189–198 (2018)
4. Capannolo, A., Lavagna, M., Ferrari, F., Lunghi, P.: Nanosatellite formation flying to enhance science in binary asteroid environment. In: 67th International Astronautical Congress (IAC), Guadalajara, Mexico, pp. 26–30 (2016)
5. Capannolo, A., Lavagna, M., Ferrari, F., Lunghi, P.: Optimal configurations for nanosatellite formation flying in binary asteroid environment. In: 26th International Symposium on Space Flight Dynamics, pp. 1–9 (2017)
6. Capannolo, A., Zanotti, G., Lavagna, M., Epifani, E.M., Dotto, E., Della Corte, V., Gai, I., Zannoni, M., Amoroso, M., Pirrotta, S.: Challenges in licia cubesat trajectory design to support dart mission science. Acta Astronautica (2020)
7. Carpenter, J.R., Souza, C.N.D.: Navigation Filter Best Practices. April. NASA (2018)
8. Chang, G.: Robust Kalman filtering based on Mahalanobis distance as outlier judging criterion. Journal of Geodesy **88**(4), 391–401 (2014). DOI 10.1007/s00190-013-0690-8
9. Cheng, A.F., Rivkin, A.S., Michel, P., Atchison, J., Barnouin, O., Benner, L., Chabot, N.L., Ernst, C., Fahnestock, E.G., Kueppers, M., et al.: Aida dart asteroid deflection test: Planetary defense and science objectives. Planetary and Space Science **157**, 104–115 (2018)
10. Dell'Elce, L., Baresi, N., Naidu, S., Benner, L., Scheeres, D.: Numerical investigation of the dynamical environment of 65803 didymos. Advances in Space Research **59**(5), 1304–1320 (2017)
11. Dotto, E., Della Corte, V., Amoroso, M., Bertini, I., Brucato, J., Capannolo, A., Cotugno, B., Cremonese, G., Di Tana, V., Gai, I., et al.: Liciacube-the light italian cubesat for imaging of asteroids in support of the nasa dart mission towards asteroid (65803) didymos. Planetary and Space Science p. 105185 (2021)
12. ESA: Asteroid impact mission: Didymos and ejecta reference model. Tech. rep., European Space Agency (2016)
13. ESA-TECSAG-TN-011315: HERA: Proximity Operations. ESA (2018)
14. Ferrari, F., Lavagna, M.: Consolidated phase a design of asteroid impact mission: Mascot-2 landing on binary asteroid didymos. In: Proceedings of AAS/AIAA Space Flight Mechanics Meeting, Napa, CA, USA (2016)
15. Ferrari, F., Lavagna, M., Carnelli, I.: Coupling high fidelity body modeling with non-keplerian dynamics to design aim-mascot-2 landing trajectories on didymos binary asteroid. In: Proceedings of the 6th International Conference on Astrodynamics Tools and Techniques, Darmstadt, DE (2016)

16. Giannitrapani, A., Ceccarelli, N., Scortecci, F., Garulli, A.: Comparison of EKF and UKF for spacecraft localization via angle measurements. IEEE Transactions on Aerospace and Electronic Systems **47**(1), 75–84 (2011). DOI 10.1109/TAES.2011.5705660
17. Gil-Fernandez, J., Ortega-Hernando, G.: Autonomous vision-based navigation for proximity operations around binary asteroids. CEAS Space Journal **10**(2), 287–294 (2018). DOI 10.1007/s12567-018-0197-5
18. Goldberg, H.R., Karatekin, O., Ritter, B., Herique, A., Tortora, P., Prioroc, C., Gutierrez, B.G., Martino, P., Carnelli, I.: The juventas cubesat in support of esa ' s hera mission to the asteroid didymos. In: 33rd Annual AIAA/USU Conference on Small Satellites (2019)
19. Grebow, D.: Generating periodic orbits in the circular restricted three-body problem with applications to lunar south pole coverage. MSAA Thesis, School of Aeronautics and Astronautics, Purdue University (2006)
20. Holger, S., Keller, H., Jaumann, R., Michalik, H., T, B., F, B., et al.: The Dawn framing camera. Space science reviews **163**(1-4), 263–327 (2011)
21. Katake, A.B.: Modeling, image processing and attitude estimation of high speed star sensors. Ph.D. thesis, Texas A&M University (2006)
22. Koon, W.S., Lo, M.W., Marsden, J.E., Ross, S.D.: Dynamical systems, the three-body problem and space mission design. California Institute of Technology, Pasadena, CA, USA (2006)
23. Liebe, C.C.: Pattern recognition of star constellations for spacecraft applications. IEEE Aerospace and Electronic Systems Magazine **7**(6), 34–41 (1992)
24. Lou, T., Fu, H., Wang, Z., Zhang, Y.: Schmidt-Kalman Filter for Navigation Biases Mitigation during Mars Entry. Journal of Aerospace Engineering **28**(4), 04014101 (2014). DOI 10.1061/(asce)as.1943-5525.0000423
25. MacMillan, W.D.: The theory of the potential. Dover (1958)
26. Naidu, S., Benner, L., Brozovic, M., Nolan, M., Ostro, S., Margot, J., Giorgini, J., Hirabayashi, T., Scheeres, D., Pravec, P., et al.: Radar observations and a physical model of binary near-earth asteroid 65803 didymos, target of the dart mission. Icarus **348**, 113777 (2020)
27. Pellacani, A., Graziano, M., Fittock, M., Gil, J., Carnelli, I.: HERA vision based GNC and autonomy. In: 8TH EUROPEAN CONFERENCE FOR AERONAUTICS AND SPACE SCIENCES (EUCASS), pp. 1–14 (2019). DOI 10.13009/EUCASS2019-39
28. Pesce, V., Losi, L., Lavagna, M.: Vision-based algorithm and robust filtering for state estimation of an uncooperative object in space. In: Proceedings of the 14th Symposium on Advanced Space Technologies in Robotics and Automation ASTRA 2017, Leiden, The Netherlands (2017)
29. Pesce, V., Opromolla, R., Sarno, S., Lavagna, M., Grassi, M.: Autonomous relative navigation around uncooperative spacecraft based on a single camera. Aerospace Science and Technology (2018). DOI 10.1016/j.ast.2018.11.042
30. Pravec, P., Scheirich, P., Kušnirák, P., Šarounová, L., Mottola, S., Hahn, G., Brown, P., Esquerdo, G., Kaiser, N., Krzeminski, Z., et al.: Photometric survey of binary near-earth asteroids. Icarus **181**(1), 63–93 (2006)
31. Riedel, J.E., Bhaskaran, S., Eldred, D.B., Gaskell, R.A., Grasso, C.A., Kennedy, B., Kubitschek, D., Mastrodemos, N., Synnott, S.P., Vaughan, A., Werner, R.A.: AutoNav Mark3: Engineering the next generation of autonomous onboard navigation and guidance. Collection of Technical Papers - AIAA Guidance, Navigation, and Control Conference 2006 **7**, 4835–4852 (2006). DOI 10.2514/6.2006-6708
32. Stone, R.C.: A comparison of digital centering algorithms. The Astronomical Journal **97**, 1227–1237 (1989)
33. Szebehely, V.: Theory of orbits: the restricted problem of three bodies. Tech. rep., Yale univ New Haven CT (1967)
34. Werner, R.A., Scheeres, D.J.: Exterior gravitation of a polyhedron derived and compared with harmonic and mascon gravitation representations of asteroid 4769 castalia. Celestial Mechanics and Dynamical Astronomy **65**(3), 313–344 (1996)